

Boosting carrier mobility in MgAgSb via in-situ InSb nanoprecipitates for high-efficiency segmented thermoelectric module

Received: 22 April 2025

Accepted: 4 August 2025

Published online: 12 August 2025

 Check for updates

Liangjun Xie^{1,2,4}, Haoyang Tong^{1,4}, Guyang Peng^{3,4}, Hao Wu¹, Wenjing Shi¹, Kuai Yu¹, Jinsuo Hu¹, Lei Jiao¹, Xingyan Dong¹, Fengkai Guo¹, Wei Cai¹, Yang Zhang³, Haijun Wu³ ✉, Zihang Liu² ✉ & Jiehe Sui¹ ✉

Carrier mobility has conventionally been manipulated to enhance thermoelectric performance by reducing crystal defects. Therefore, an effective strategy for optimizing carrier mobility is highly desired for nanostructured materials. In this work, InSb nanoprecipitates are formed in situ within the nanostructured MgAgSb matrix, serving as channels for accelerating charge carriers. A high carrier mobility of $93.1 \text{ cm}^2 \text{ V}^{-1} \text{ s}^{-1}$ is achieved in $\text{MgAg}_{0.97}\text{Sb}_{0.99}\text{-}0.02\text{InSb}$ composite at 300 K, resulting in an average power factor of $23.8 \text{ } \mu\text{W cm}^{-1} \text{ K}^2$ from 300 K to 553 K. To address the efficiency degradation caused by the narrow operational temperature range of MgAgSb, a two-pair segmented thermoelectric module is developed. A high conversion efficiency of 12.4% is achieved under a cold-side temperature of -293 K and a temperature difference of $\sim 540 \text{ K}$, presenting an effective strategy for carrier mobility optimization and opening new avenues for medium-temperature waste heat harvesting using MgAgSb.

Thermoelectric (TE) technology enables the direct and reversible conversion between thermal and electrical energy and serves as an attractive approach for waste heat recovery and solid-state cooling^{1,2}, owing to its distinctive advantages of long-term robustness³, miniaturization⁴, and precise temperature control⁵. Theoretically, the conversion efficiency (η) of a TE module is determined by the average dimensionless figure of merit (ZT_{ave}) of material over the operating temperature range between the hot (T_H) and cold (T_C) sources, as follows:

$$\eta = \frac{T_H - T_C}{T_H} \frac{\sqrt{1 + ZT_{\text{ave}}} - 1}{\sqrt{1 + ZT_{\text{ave}}} + T_C/T_H} \quad (1)$$

where ZT_{ave} is expressed as:

$$ZT_{\text{ave}} = \frac{1}{T_H - T_C} \int_{T_C}^{T_H} ZT dT \quad (2)$$

The temperature-dependent dimensionless figure of merit ZT is given by $ZT = S^2 T / (\rho \kappa)$, where S , ρ , κ , and T are the Seebeck coefficient, electrical resistivity, thermal conductivity, and absolute temperature (in Kelvin), respectively. Typically, ρ is governed by carrier concentration (n) and carrier mobility (μ), while κ comprises both lattice thermal conductivity (κ_L) and electrical thermal conductivity (κ_e). Therefore, it follows from the above expression that maximizing ZT over a broad temperature range is crucial for achieving high TE conversion efficiency^{6–8}.

Ideally, a high-performance TE material should simultaneously exhibit a well-ordered crystal structure to facilitate electron transport and a disordered architecture to scatter phonons of various wavelengths—a concept known as the ‘phonon glass-electron crystal’^{9,10}. However, the intricate interrelations between TE parameters (S , ρ , and κ) make achieving a high ZT value in practice challenging. Fortunately, κ_L and μ , as two relatively independent parameters, have been intensively manipulated to enhance the ZT of materials¹¹. Defect engineering

¹National Key Laboratory for Precision Hot Processing of Metals, Harbin Institute of Technology, Harbin, China. ²State Key Laboratory of Advanced Welding and Joining, Harbin Institute of Technology, Harbin, China. ³State Key Laboratory for Mechanical Behavior of Materials, Xi’an Jiaotong University, Xi’an, China.

⁴These authors contributed equally: Liangjun Xie, Haoyang Tong, Guyang Peng. ✉ e-mail: wuhaijunnavy@xjtu.edu.cn; zihangliu@hit.edu.cn; suijiehe@hit.edu.cn

is a widely adopted approach to reduce κ_L by enhancing phonon scattering^{12,13}. However, the introduction of defects often hinders carrier transport, leading to a significant reduction in carrier mobility in nanostructured TE materials, thereby limiting the improvement of ZT . Eliminating carrier scattering through manipulation of crystal defects involves strategies such as crystal growth and crystal symmetry manipulation, which have shown great potential for enhancing thermoelectric performance^{14–16}.

In the low-temperature range, α -MgAgSb has emerged as a promising alternative to p-type Bi_2Te_3 , attracting significant attention due to its inherently low lattice thermal conductivity, which stems from complex microstructure, as well as its excellent electrical transport properties arising from high energy band degeneracy^{17–19}. However, the inherent irreversibility of phase transitions limits the applicability of crystal growth methods for optimizing carrier mobility. Fortunately, the two-phase hybridization effect, which strategically incorporates a secondary phase with intrinsically high-carrier mobility to facilitate charge carrier transport, offers a compelling approach to enhancing the thermoelectric performance of composite materials. This approach has undergone extensive validation across a diverse range of composite materials, including Half-Heusler^{20,21} and skutterudite²² composites incorporating InSb, BiCuSeO ²³, GeTe ²⁴, Bi_2Te_3 ²⁵, and

Mg_3Sb_2 ^{26,27} composites incorporating single-wall carbon nanotubes (SWCNTs). Moreover, due to the low phase transition temperature of α -MgAgSb ($\sim 600\text{ K}$)^{28–30}, the remarkable ZT of α -MgAgSb can only be sustained within a narrow operational window from room temperature to approximately 573 K , thereby restricting the viable temperature range of MgAgSb-based TE power generators^{31,32}. To address this limitation, the development of segmented TE modules, which integrate materials with high ZT at their respective optimal operating temperatures, has emerged as an effective strategy.

Herein, inspired by the two-phase hybridization effect and guided by the quaternary phase diagram (Fig. S1), a high-carrier-mobility InSb secondary phase was in situ formed within the MgAgSb matrix. Acting as an acceleration channel for charge carriers (Fig. 1A), the InSb nanoprecipitates significantly enhance carrier mobility, which in turn boosts the TE performance of composites. As shown in Fig. 1B, a high-carrier mobility of $93.1\text{ cm}^2\text{ V}^{-1}\text{ s}^{-1}$ was achieved in $\text{MgAg}_{0.97}\text{Sb}_{0.99}\cdot 0.02\text{InSb}$ composite at room temperature, which is notably higher than that of the previously reported ball-milled samples^{33–40}, resulting in a high average power factor (PF_{ave}) of $23.8\text{ }\mu\text{W cm}^{-1}\text{ K}^{-2}$ at a relatively low carrier concentration and a high average figure of merit (ZT_{ave}) of 1.1 from 300 to 553 K . To further extend the operating temperature range of MgAgSb and achieve higher conversion efficiency, a MgAgSb-

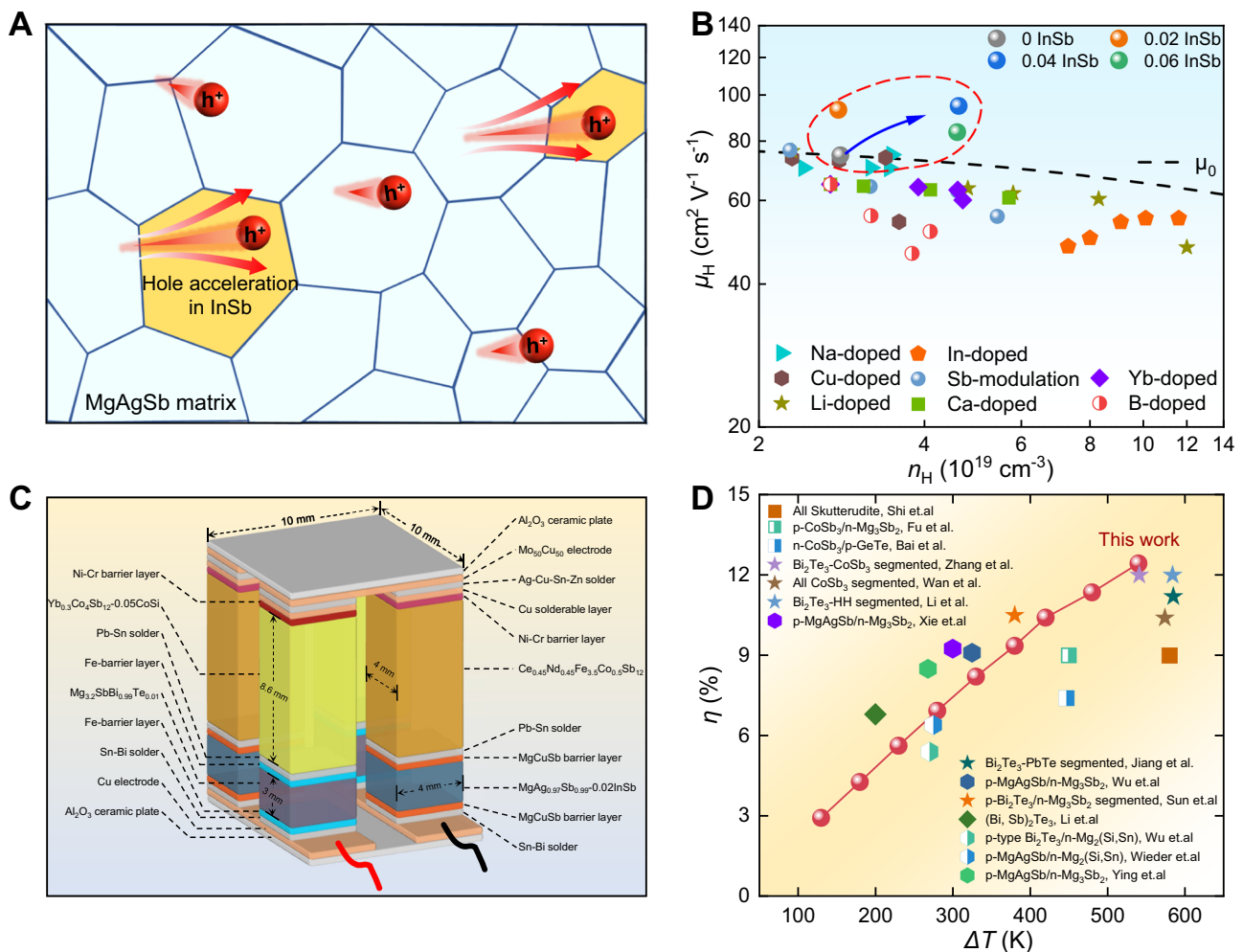


Fig. 1 | Carrier mobility optimization and segmented module of MgAgSb.

A Schematic illustration of hole acceleration in MgAgSb-InSb composites based on the two-phase hybridization effect. **B** Carrier mobility as a function of carrier concentration for InSb-composited and element-doped MgAgSb samples^{33–40}. **C** Schematic diagram of a segmented thermoelectric module composed of p-type MgAgSb and n-type $\text{Mg}_{3.2}\text{SbBi}$ as low-temperature sections, and p- and n-type

skutterudite as high-temperature sections. **D** Temperature difference (ΔT) dependence of the maximum conversion efficiency (η_{max}) of the MgAgSb/skutterudite segmented module. For comparison, the performance of several low-temperature Bi_2Te_3 -based^{41,42}, MgAgSb/Mg₃(Sb, Bi)₂^{32,43–45}, and skutterudite-based modules^{46–48}, and various segmented modules^{49–53} were also presented.

based segmented TE module was designed for the first time (Fig. 1C), with p-type MgAgSb and n-type $\text{Mg}_{3.2}\text{SbBi}$ as the low-temperature section, and p-type and n-type skutterudites as the high-temperature section. Benefiting from the enhanced TE performance of p-type MgAgSb through carrier mobility optimization and reasonable module geometry, a high maximum conversion efficiency of 12.4 % was achieved at $T_C = 293\text{ K}$ and $\Delta T = 540\text{ K}$ (Fig. 1D). This performance surpasses that of classical Bi_2Te_3 -based^{41,42}, Mg-based^{32,43–45}, and skutterudite-based^{46–48} single-stage TE modules, as well as several segmented TE modules^{49–53}, demonstrating great potential for waste heat recovery in the medium-temperature range.

Results and discussion

To investigate the phase structure of the composites, powder X-ray diffraction (PXRD) measurements were performed on $\text{MgAg}_{0.97}\text{Sb}_{0.99-x}\text{InSb}$ ($x = 0, 0.02, 0.04, \text{ and } 0.06$) samples, as shown in Fig. S2. The PXRD patterns of all samples exhibit excellent agreement with the calculated diffraction pattern. Nevertheless, although the Mg–Ag–Sb–In quaternary phase diagram predicts the formation of the InSb phase in the composites (Fig. S1), no distinct diffraction peaks corresponding to InSb were detected, which is likely attributed to the substantial overlap between the diffraction peaks of InSb and those of $\alpha\text{-MgAgSb}$. Therefore, Rietveld refinement was performed to determine the lattice parameters of MgAgSb and the volume fraction of InSb (Fig. S3). As presented in Fig. S4A, both lattice parameters a and c of the MgAgSb phase decrease with increasing InSb content, suggesting the possible formation of Ag vacancies within the MgAgSb lattice rather than the substitution of In at Sb sites. This inference arises from the relatively larger ionic radius of In^{3+} (0.08 nm) compared to Sb^{3+} (0.076 nm)⁵⁴. In addition, the volume fraction of InSb increases from 1.18% to 1.99% and 2.81% as x increases from 0.02 to 0.04 and 0.06 (Fig. S4B). Scanning electron microscope (SEM) analysis was further employed to investigate the sample microstructure. The fresh fracture morphology of all samples (Fig. S5) shows that the addition of InSb did not significantly affect the grain size. Energy-dispersive spectroscopy (EDS) mapping indicates that all elements are uniformly distributed within the sample, even when the InSb content reaches 6% (Fig. S6).

Due to resolution limitations, PXRD and low-magnification SEM could not precisely characterize the InSb nanoprecipitates within the matrix. Therefore, high-resolution scanning transmission electron microscopy (HRSTEM) was employed to directly investigate the phase distribution, structure, and morphology of the composites. Figure 2A presents the high-angle annular dark-field (HAADF) image of the $\text{MgAg}_{0.97}\text{Sb}_{0.99-0.02}\text{InSb}$ composite, where uniformly distributed nanoprecipitates containing In, Sb, and trace concomitant occurrences of Ag are distinguishable, as confirmed by EDS mapping (Fig. 2B). A magnified region from Fig. 2A, encompassing both In–Sb and Ag–In enriched phases (Fig. S7), is shown in Fig. 2C to meticulously characterize the phase structures and boundaries in detail. As expected, the In–Sb enriched phase in Fig. 2D was identified as InSb through Fast Fourier Transform (FFT) analysis (Fig. 2D2). Notably, the FFT image reveals four distinct peaks near the InSb (020) reflection, and further analysis confirms that these features arise from the presence of multiple nanoscale crystallographic orientations (Fig. S8). However, owing to the pronounced lattice mismatch between MgAgSb and InSb, an ideal coherent or semi-coherent interface fails to form at the phase boundaries. Consequently, when charge carriers transport across these interfaces, interfacial scattering occurs. This contributes to the observed saturation or even reduction in carrier mobility with increasing InSb content, as discussed in detail below. The In–Ag enriched phase in Fig. 2E corresponded to Ag_3In (Fig. 2E2). Notably, the phase boundary between InSb and Ag_3In was determined to be coherent, suggesting minimal carrier scattering at the two-phase boundary. To further validate the presence of InSb in the MgAgSb matrix, an additional In–Sb-rich precipitate from Fig. 2C was

scrutinized (Fig. 2F). Both the HRSTEM images and corresponding atomic structural model (Fig. 2G, H) unequivocally confirmed the formation of InSb nanoprecipitates. These findings indicate that the incorporation of In–Sb into MgAgSb leads to the spontaneous formation of uniformly distributed InSb nanoprecipitates during mechanical alloying and hot press sintering. Simultaneously, a small amount of In reacts with Ag, forming a trace Ag_3In phase, which increases the concentration of Ag vacancies and results in a slight reduction in the lattice parameters of MgAgSb.

Figure 3 illustrates the TE properties of $\text{MgAg}_{0.97}\text{Sb}_{0.99-x}\text{InSb}$ ($x = 0, 0.02, 0.04, \text{ and } 0.06$) composites. As shown in Fig. 3A, B, both the electrical resistivity (ρ) and Seebeck coefficient (S) of all samples increase with temperature and then decrease at higher temperatures due to intrinsic excitation. Meanwhile, the in situ formation of InSb within the MgAgSb matrix leads to a noticeable reduction in both ρ and S , especially near the room temperature region. Specifically, ρ decreases from $-29.72\ \mu\Omega\text{ m}$ for $x = 0$ to $-14.27\ \mu\Omega\text{ m}$ for $x = 0.04$ at 300 K, while the S decreases from $-241.09\ \mu\text{V K}^{-1}$ to $-188.05\ \mu\text{V K}^{-1}$. To further elucidate the factors that contribute to alterations in electrical transport properties, the room temperature carrier concentration (n_H) and carrier mobility (μ_H) of all samples were measured. As shown in Fig. 3C, the n_H remains nearly unchanged for the 0.02InSb composite. However, it slightly increases from $-2.82 \times 10^{19}\text{ cm}^{-3}$ for the pristine sample to $-4.59 \times 10^{19}\text{ cm}^{-3}$ for the $x = 0.04$ sample with increasing InSb content. This suggests that the InSb precipitates have minimal impact on the doping level of the matrix. The observed increase in n_H is likely attributed to the proliferation of Ag vacancies within the MgAgSb phase, triggered by the formation of a trace amount of the Ag_3In secondary phase, as evidenced by XRD and HRTEM results. Simultaneously, μ_H exhibits a significant enhancement with increasing InSb content. At room temperature, the μ_H increases from $-74.7\text{ cm}^2\text{ V}^{-1}\text{ s}^{-1}$ for the pristine sample to $93.1\text{ cm}^2\text{ V}^{-1}\text{ s}^{-1}$ for the 0.02InSb composite, as the InSb content further increases, a maximum μ_H of $-94.8\text{ cm}^2\text{ V}^{-1}\text{ s}^{-1}$ is observed at 0.04InSb composite, followed by a decrease to $83.5\text{ cm}^2\text{ V}^{-1}\text{ s}^{-1}$ for the 0.06InSb composite, indicating that two competing effects govern the mobility in the composite materials. On the one hand, the formation of the intrinsically high-mobility InSb phase accelerates the charge transport. On the other hand, increased concentration of Ag vacancies, the formation of $\text{Ag}_3\text{In}/\text{MgAgSb}$ and InSb/MgAgSb phase boundaries, as well as enhanced carrier–carrier scattering, contribute to the degradation of mobility. Nevertheless, even at its lowest, the mobility of the composites remains significantly higher than that of the pristine sample.

According to the two-phase hybridization effect, both the intrinsic electrical properties of the secondary phase and the carrier transport behavior at the phase boundaries play crucial roles in determining the carrier mobility of composites. In particular, the formation of an energy barrier at the interface is a key factor influencing carrier transport, especially when the interface is formed between two semiconductors. Therefore, it is essential to evaluate the semiconducting nature of the secondary phase. In our composites, InSb is embedded in an Ag- and Mg-rich environment, where Ag and Mg may incorporate into the InSb lattice and alter its properties. Literature reports indicate that Ag doping in InSb has a negligible effect on its semiconductor nature⁵⁵. In contrast, Zn, which exhibits a similar doping effect to Mg in TE materials, can be readily doped into InSb, effectively converting InSb into a p-type semiconductor⁵⁶. Therefore, the TE properties of Mg-doped InSb were thoroughly investigated. As illustrated in Fig. S9, a small amount of incorporated Mg converts InSb into a p-type semiconductor. Furthermore, nanostructured p-type $\text{Mg}_{0.005}\text{In}_{0.995}\text{Sb}$ exhibits a carrier mobility of $212.5\text{ cm}^2\text{ V}^{-1}\text{ s}^{-1}$ at room temperature, which remains superior to that of MgAgSb across the entire temperature range, as shown in Fig. S10. This suggests that no phase boundary with a significant energy barrier is formed between p-type MgAgSb and p-type InSb. Consequently, the uniformly distributed

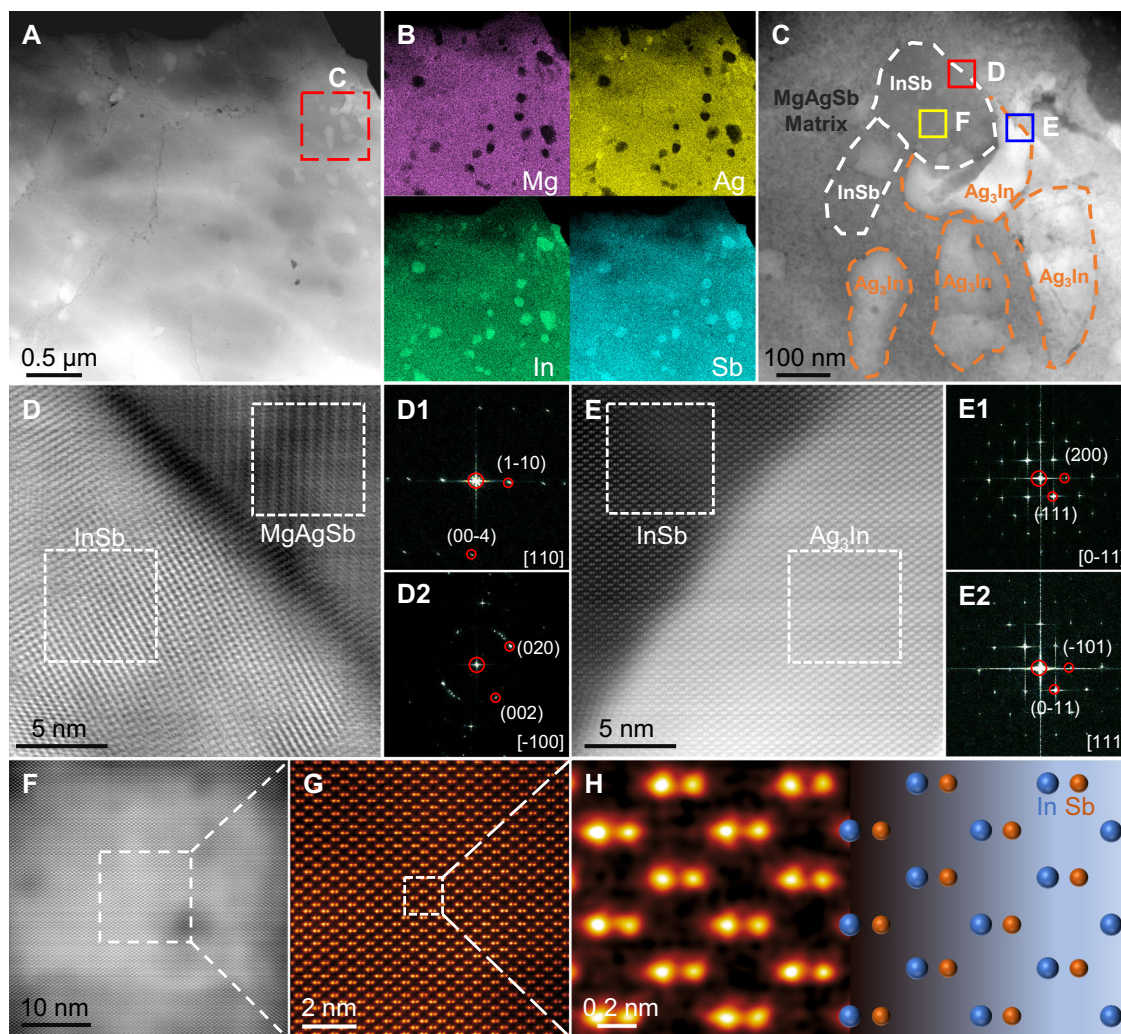


Fig. 2 | STEM characterization of the $\text{MgAg}_{0.97}\text{Sb}_{0.99}\text{-0.02InSb}$ composite. **A** HAADF-STEM image. **B** Corresponding EDS mapping of **(A)**. **C** HAADF image of the area enclosed by the red box in **(A)**, with InSb and Ag_3In nanoprecipitates outlined by white and orange dashed lines, respectively. **D, E** High-magnification TEM images from **(C)**, showing InSb-MgAgSb and InSb- Ag_3In phase boundaries. The

corresponding FFT images were indexed as MgAgSb (**D1**), InSb (**D2** and **E1**), and Ag_3In (**E2**), respectively. **F** Atomic-resolution HAADF image of the InSb secondary phase along the [111] crystallographic direction. **G, H** Magnified views of **(F)** with the corresponding atomic structural model.

InSb phase within composites serves as an acceleration channel for carriers, effectively enhancing the μ_{H} of the composites and potentially leading to a further foreseeable increase in PF .

In addition to the scattering of carriers during transport by phonons and defects, the effective mass (m^*) of the carrier is another key factor that significantly affects μ_{H} . To investigate this, a Pisarenko line depicting the relationship of n_{H} and S at room temperature was fitted using the single parabolic band (SPB) model, based on acoustic phonon scattering mechanisms, as plotted in Fig. S11. The m^* of the pristine sample at 300 K is $1.76 m_{\text{e}}$ (m_{e} is the free electron mass), which is comparable to the previously reported m^* values. Moreover, the m^* of composites shows no significant deviation from the line upon the incorporation of InSb, indicating that the increased μ_{H} is not due to a reduction in m^* and the band structure of MgAgSb remains largely unaltered. The weighted mobility (μ_{wt}), which elucidates the electronic structure and scattering mechanisms in materials, is calculated and depicted in Fig. 3D. The μ_{wt} curves for all samples display an exponential decrease with temperature, following a $T^{-1.5}$ dependence in the low-temperature range, indicating that acoustic phonon scattering dominates. Additionally, a consistent increase in μ_{wt} across the entire temperature range is observed after the formation of InSb in the composites. Combining these two results, we conclude that the

primary mechanism governing carrier scattering is not altered by the in situ formation of InSb nanoprecipitates. Therefore, the optimized carrier transport mechanism is driven by the two-phase hybridization effect, rather than grain boundary scattering elimination, which contrasts with the mechanism observed in $\text{Mg}_2(\text{Sb}, \text{Bi})_2$ -based materials^{57,58}. As a result of the independent increases in μ_{H} , the trade-off relationship between PF and n_{H} is decoupled (Fig. S12). Consequently, the PF increases from $19.53 \mu\text{W cm}^{-1} \text{K}^{-2}$ for the $x = 0$ sample to $24.79 \mu\text{W cm}^{-1} \text{K}^{-2}$ for the $x = 0.04$ sample at 300 K (Fig. 3E). Notably, a maximum average power factor (PF_{ave}) value of $23.84 \mu\text{W cm}^{-1} \text{K}^{-2}$ is achieved for the $x = 0.04$ sample across the 300-550 K range (Fig. S13). The thermal conductivity (κ) of MgAgSb-InSb composites shows a moderate increase between 300 and 550 K compared to the pristine sample, as depicted in Fig. S14. This phenomenon can be primarily attributed to the simultaneous rise in both electrical thermal conductivity (κ_{e}) and lattice thermal conductivity (κ_{l}), as illustrated in Fig. S15. The underlying reason can be attributed to the ultrahigh κ_{l} of InSb. Overall, despite the increase in κ of the composites, a maximum ZT of 0.86 at 300 K (Fig. 3F) and ZT_{ave} of 1.15 over 300-550 K (Fig. S13) are realized in $\text{MgAg}_{0.97}\text{Sb}_{0.99}\text{-0.02InSb}$.

To further extend the operating temperature range of MgAgSb to elevated temperatures, overcoming the limitations imposed by its low

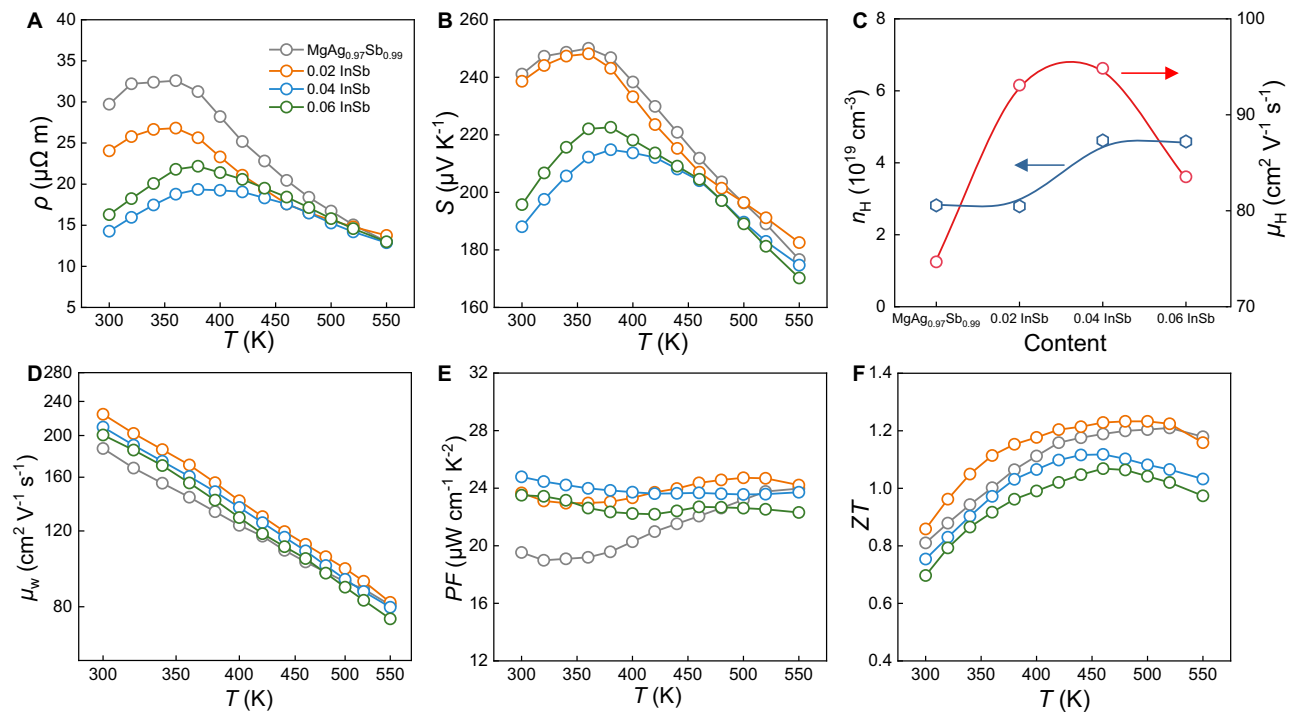


Fig. 3 | Thermoelectric properties of $\text{MgAg}_{0.97}\text{Sb}_{0.99-x}\text{InSb}$ composites. **A, B** Temperature dependence of electrical resistivity (ρ) and Seebeck coefficient (S), respectively. **C** Room temperature carrier concentration (n_{H}) and mobility (μ_{H}).

D, E, F Temperature dependence of weighted mobility (μ_{w}), power factor (PF), and figure of merit (ZT), respectively.

phase transition temperature is essential. Meanwhile, extensive research conducted over the past decade on the TE properties of skutterudites⁵⁹ and n-type $\text{Mg}_3(\text{Bi}, \text{Sb})_2$ ^{60,61}, as well as their barrier layers^{43,48,62}, has enabled the development of advanced segmented modules. Consequently, a two-pair segmented TE module was developed, consisting of optimized p-type $\text{MgAg}_{0.97}\text{Sb}_{0.99-0.02}\text{InSb}$ from this work and n-type $\text{Mg}_{3.2}\text{SbBi}$ as low-temperature components, with p- and n-type skutterudites as high-temperature components. Further details regarding the TE performance of these materials (Fig. S16) and preparation of the segmented TE module can be found in the Methods. To optimize the module performance over its operational temperature range, a series of calculations was performed based on the material properties at a cold-side temperature (T_{h}) of 293 K with a temperature difference (ΔT) of 540 K. In these calculations, the cross-sectional area of each leg was set to $4 \times 4 \text{ mm}^2$ to achieve a higher fill factor for the module, thereby reducing thermal convection and radiation within the module⁶³. As shown in Fig. 4A, an enhanced theoretical maximum conversion efficiency (η_{max}) is achieved by increasing the proportion of the low-temperature sections of the p-type (R_{p}) and n-type (R_{n}) legs relative to the total leg length. Nevertheless, a pivotal yet often disregarded aspect is the temperature distribution at the segmented interface, which significantly affects the stability of the module. If the temperature at the segmented interface exceeds the threshold that the material in the low-temperature section can withstand, the module becomes highly susceptible to damage. This is a particular concern for MgAgSb , which is prone to phase transition. As illustrated in Fig. S18, the temperature at the p-type segmented interface is predicted to remain below 573 K (the stable service temperature of MgAgSb) when R_{p} is less than 0.28, and the R_{n} should be less than 0.3 for the n-type legs. Consequently, the lengths of the p-type MgAgSb and Skutterudite segmented legs were designed to be 3 mm and 8.6 mm, respectively, with the same design applied to the n-type segmented legs to ensure ease of fabrication. Based on the simulated module geometry, we further calculated the theoretical conversion efficiency (η) and output power (P) of the segmented module as a function of InSb content in the

p-type low-temperature segment, under identical geometric and temperature conditions. As shown in Fig. S19, a maximum theoretical P of 1.32 W and a high η of 17.03% are achieved for the $x=0.02$ InSb-segmented module, both of which are higher than those of the $x=0$ module (1.28 W and 16.88%, respectively). These results indicate that the performance enhancement of the segmented module indeed originates from the improved ZT induced by the introduction of InSb. Consistent with the simulation results, the p- and n-type segmented legs were fabricated and joined to measure the contact resistivity and evaluate the quality of the joints. As illustrated in Fig. 4B, no notable jump in contact resistivity (R_{c}) was observed at any of the connecting interfaces as the test probe was moved, indicating that high-quality contact and joining layers were successfully achieved (Detailed R_{c} values of four interfaces are provided in Fig. S17 and Table S1). Moreover, all R_{c} curves in the materials section were linear, and the resistivity values calculated from the R_{c} curves showed excellent correlation with those obtained using the four-probe method via ZEM-3. This suggests that the sintered materials with barrier layers are internally homogeneous and exhibit minimal changes in TE properties.

The output power and conversion efficiency of the segmented TE module were measured by varying the current (I) under different temperature differences (ΔT) with a fixed cold-side temperature (T_{c}) of $\sim 293 \text{ K}$. Meanwhile, the theoretical performance of the segmented module was calculated under the same ΔT for comparison and analysis (Fig. S20). As illustrated in Fig. 5A, the measured series of voltage-current ($V-I$) curves exhibited a satisfactory linear correlation. The inner resistance R_{in} of the module was determined from these $V-I$ curves, with a slight deviation from the theoretical values (Fig. 5B). This discrepancy is likely due to additional inner resistance introduced during the soldering or contact resistance during the module measurement. Moreover, the unavoidable interface thermal resistance resulting from the imperfect contact between the TE module and the heat/cold sources leads to a reduction in the effective ΔT across the TE module, with this discrepancy increasing in line with rising ΔT . Consequently, as depicted in Fig. 5C, the divergence between the

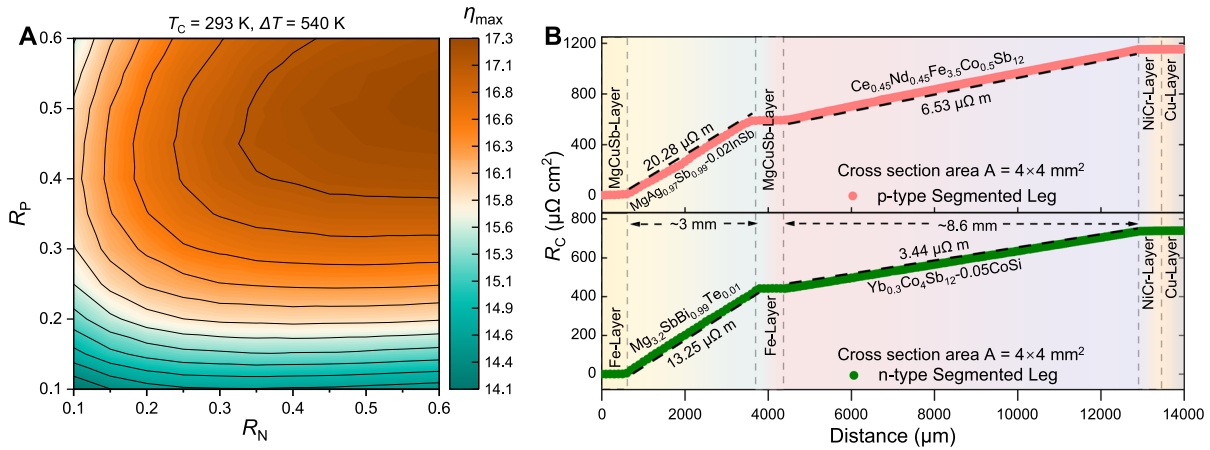


Fig. 4 | Optimized module geometry and measured contact resistivity. **A** Calculated maximum conversion efficiency (η_{\max}) of MgAgSb/Skutterudite segmented TE module as a function of the ratio of the low-temperature portion of the

p-type (R_P) and n-type (R_N) legs to the total leg length. **B** Measured contact resistivity (ρ_c) of n-type and p-type segmented legs.

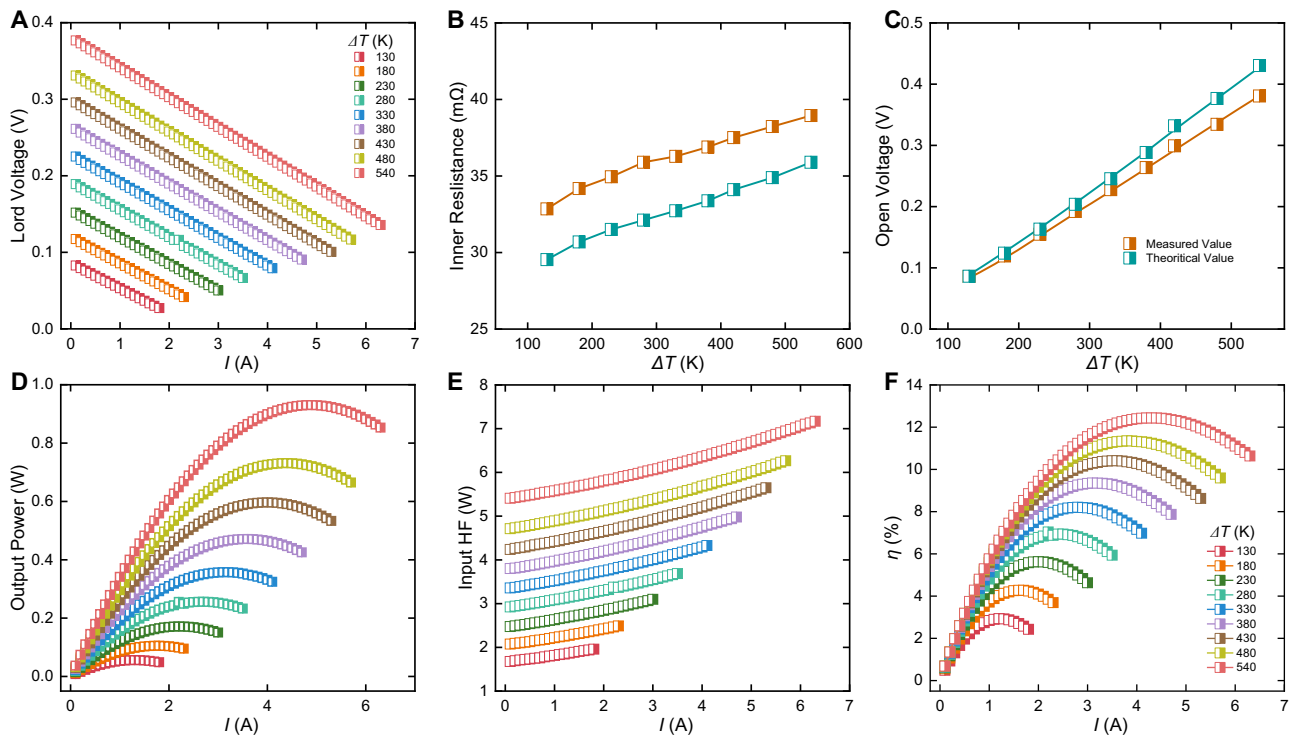


Fig. 5 | Power generation performance of the MgAgSb/skutterudite segmented module. **A** Current (I) dependence of the lord voltage (U). **B**, **C** Temperature difference (ΔT) dependence of measured and simulated inner resistance (R_{in}) and

open-circuit voltage (V_{oc}). **D**, **E**, **F** Current (I) dependence of output power (P), output heat flow (Q), and conversion efficiency (η) for the Mg-based/skutterudite segmented module at a cold-side temperature of -293 K.

theoretical and actual open-circuit voltage (V_{oc}) of the module becomes increasingly pronounced. Figure 5D shows the P of the module at varying ΔT . The actual maximum output power (P_{\max}) reaches 0.93 W with a ΔT of -540 K (Fig. S20B) due to the negative effects of additional inner resistance and interface thermal resistance. Similarly, the measured output heat flow (Q) was progressively higher than the theoretical values (Fig. S21), which can be attributed to the increased thermal radiation and convection between the hot and cold sides of the module—another significant factor that impairs the actual performance of the module. Ultimately, a maximum conversion efficiency

(η_{\max}) of 12.4% was achieved at $T_C = 293$ K and $\Delta T = 540$ K (Fig. 5F). This indicates that further optimization of the soldering process, elimination of interface thermal resistance, and isolation of thermal radiation and convection will enable higher power generation performance in future iterations.

In conclusion, an effective strategy for optimizing carrier mobility in α -MgAgSb was successfully established, enabling the development of a high-performance two-pair MgAgSb/Skutterudite segmented TE module with excellent conversion efficiency. The in situ formation of InSb nanoprecipitates with intrinsically high-carrier mobility within the MgAgSb matrix was demonstrated to markedly enhance carrier

transport, achieving a high-carrier mobility of $93.1 \text{ cm}^2 \text{ V}^{-1} \text{ s}^{-1}$ in the $\text{MgAg}_{0.97}\text{Sb}_{0.99}\text{-}0.02\text{InSb}$ composite at 300 K. As a result of enhanced carrier mobility over the entire temperature range, the $\text{MgAg}_{0.97}\text{Sb}_{0.99}\text{-}0.02\text{InSb}$ composite exhibited a PF_{ave} of $23.8 \mu\text{W cm}^{-1} \text{ K}^{-2}$ and a ZT_{ave} of 1.1 between 300 K and 553 K. Furthermore, integrating skutterudite as the high-temperature segment in the $\text{MgAgSb/Skutterudite}$ TE module successfully overcomes the limitations imposed by the phase transition of MgAgSb , thereby extending its applicable temperature range. Ultimately, the synergy between the enhanced TE performance of MgAgSb , the optimized module geometry, and the well-engineered contact layers of the four constituent materials yields a notable conversion efficiency of 12.4% under $T_{\text{C}} = 293 \text{ K}$ and $\Delta T = 540 \text{ K}$. This work not only provides a practical and effective approach for optimizing carrier transport in MgAgSb -based thermoelectric materials but also offers a viable strategy for their application in mid-temperature waste heat recovery.

Methods

Materials

$\text{MgAg}_{0.97}\text{Sb}_{0.99}\text{-}x\text{InSb}$. The samples with stoichiometric compositions $\text{MgAg}_{0.97}\text{Sb}_{0.99}\text{-}x\text{InSb}$ ($x = 0, 0.02, 0.04, \text{ and } 0.06$) were prepared using a two-step ball milling process followed by Hot Press Sintering (HPS). The Magnesium (Mg) pieces (99.99%, Aladdin) and Silver (Ag) particles (99.999%, Aladdin) were first loaded into a stainless-steel jar in an argon-filled glove box and then ball-milled for 10 h. Afterwards, the Antimony (Sb) particles (99.99%, Alfa Aesar) and/or Indium (In) particles (99.999%, Alfa Aesar) were added into the jar under an argon atmosphere with another ball milling of 10 h. The obtained powder was loaded into a graphite die with an inner diameter of 12.7 mm and sintered using HPS at 573 K for 30 min. After that, the as-prepared samples were annealed at the corresponding sintering temperature for 30 min to characterize microstructures and measure properties.

$\text{Mg}_{3.2}\text{Sb}_1\text{Bi}_{0.995}\text{Te}_{0.005}$. The samples with stoichiometric compositions $\text{Mg}_{3.2}\text{Sb}_1\text{Bi}_{0.995}\text{Te}_{0.005}$ were prepared with ball milling followed by HPS. The Mg pieces, Bismuth (Bi) particles (99.999%, Aladdin), Sb particles, and Tellurium (Te) powder (99.999%, Alfa Aesar) were loaded into a stainless-steel jar in the argon-filled glove box and then ball-milled for 5 h. Afterwards, the obtained powder was loaded into a graphite die with an inner diameter of 12.7 mm and sintered using HPS at 1073 K for 20 min.

$\text{Mg}_x\text{In}_{1-x}\text{Sb}$ ($x = 0, 0.005, 0.01$). High-purity raw materials Mg pieces, Sb particles, and In particles were weighed according to the corresponding chemical composition and then added into the carbon crucible, which was then sealed in a quartz tube under vacuum, slowly heated to 1073 K and maintained for 6 h and then cooled to room temperature. The ingots obtained were loaded into a stainless-steel jar inside an argon-filled glove box, where they were ball milled for 2 h. Afterwards, the obtained powder was loaded into a graphite die with an inner diameter of 12.7 mm and sintered using HPS at 673 K for 30 min. The obtained bulk materials were cut and polished for thermoelectric characterization.

Skutterudites

High-purity raw materials Cobalt (Co) pieces (99.95%, Alfa Aesar), Sb particles, Ytterbium (Yb) ingots (99.9%, Alfa Aesar), Silicon (Si) pieces (99.9999%, Alfa Aesar), Cerium (Ce) ingots (99.8%, Alfa Aesar), Neodymium (Nd) ingots (99.8%, Alfa Aesar), and Iron (Fe) ingots (99.99%, Alfa Aesar) were weighed according to the chemical composition of $\text{Yb}_{0.3}\text{Co}_4\text{Sb}_{12}/0.05\text{CoSi}$ and $\text{Ce}_{0.45}\text{Nd}_{0.45}\text{Fe}_{3.5}\text{Co}_{0.5}\text{Sb}_{12}$ and then placed in the carbon crucible which is then sealed in a quartz tube under vacuum, slowly heated to 1423 K and maintained for 3 h and then cooled to room temperature. The reacted ingot was cleaned and placed in a quartz tube with a fine nozzle, which was induction-melted

and injected onto the copper wheel with a rotating speed of 4000 rpm under a high-purity Ar atmosphere. The obtained ribbons, droplets, and pieces were ground into fine powders in the glove box and densified using the hot-pressing method at a fixed temperature (923 K for p-type and 1023 K for n-type skutterudite) for 1 h in a 12.7 mm diameter graphite die under an axial pressure of 80 MPa.

Sample characterization and measurement

XRD. Initial phase characterization of $\text{MgAg}_{0.97}\text{Sb}_{0.99}\text{-}x\text{InSb}$ ($x = 0, 0.02, 0.04, \text{ and } 0.06$) composites was carried out by X-ray diffraction at room temperature. Finely crushed powder ($\sim 2 \text{ g}$) from the as-sintered pellets was used for X-ray analysis in the X'Pert PANalytical instrument using $\text{Cu K}\alpha$ wavelength of 1.5418 \AA and step size 0.01° from 10° to 100° . Rietveld refinement was performed on the powder XRD data with FullProf software.

SEM. The morphological, structural, and chemical characteristics of the sintered pellets were examined using a scanning electron microscope (SEM, Helios Nanolab 600i) equipped with an energy-dispersive X-ray spectroscopy (EDS) detector. To evaluate grain size, fresh fracture surfaces were imaged in secondary electron (SE) mode at an accelerating voltage of 20 kV and beam current of 0.69 nA, a working distance of 6.3 mm, and a magnification of $160,000\times$. For phase composition analysis, the sample surfaces were mechanically polished using successive grades of sandpaper followed by diamond paste, then cleaned in anhydrous ethanol using ultrasonication. The polished surfaces were subsequently characterized in back-scattered electron (BSE) mode under an accelerating voltage of 20 kV, with a working distance of 6.1 mm and a magnification of $10,000\times$.

STEM

Sample preparation. STEM specimens of $\text{MgAg}_{0.97}\text{Sb}_{0.99}\text{-}0.02\text{InSb}$ were prepared using conventional mechanical thinning followed by argon ion milling. Briefly, the process included the following steps: (i) Bulk samples were cut into approximately $2.5 \times 2.5 \times 1 \text{ mm}$ pieces with wire cutting. (ii) These pieces were polished successively using SiC abrasive papers (#400, #800, #1000, #2000, and #4000 grit) followed by a final polish with a 6000-grit colloidal silica suspension. Polishing continued until a mirror-like, scratch-free surface was achieved, resulting in a final thickness of about $30 \mu\text{m}$. (iii) The polished samples were mounted onto 3-mm molybdenum support rings with a special thermosetting adhesive and cured at 120°C for 20 min. (iv) Final thinning to electron transparency was performed with an ion beam milling system through a stepwise protocol: 5° incidence angle, 4 kV voltage, 30 min (to remove residual adhesive and surface polish); 8° incidence angle, 4 kV, until electron transparency was detected ("flashing behavior"); 6° incidence angle, 2 kV, continued until perforation occurred; 4° incidence angle, 0.5 kV (for low-angle milling, final cleaning, and minimizing ion beam damage layers).

STEM imaging. High-angle annular dark-field (HAADF) and annular bright-field (ABF) scanning transmission electron microscopy (STEM) images were obtained using a JEM-ARM300F2 microscope equipped with a cold field-emission gun (CFEG) and double probe aberration correctors (both condenser and objective lens systems with 12-pole aberration correctors). This setup offers sub-ångström resolution at 300 kV. The probe convergence semi-angle was set to 26 mrad during imaging. HAADF signals were collected over an angular range of $65\text{--}200 \text{ mrad}$, while ABF signals were captured within $13\text{--}26 \text{ mrad}$.

Image processing. The STEM images were processed after acquisition to improve signal-to-noise ratio (SNR). For low-magnification images, a single application of a two-dimensional Wiener filter was used. For high-resolution atomic images, 10 frames were acquired, aligned, averaged, and processed with the same Wiener filtering technique. The

images in Fig. 2D, E, F, G were subjected to average background subtraction and filtering to improve contrast. The EDX was operated at an acceleration voltage of 300 kV with a probe current of 1 nA. The collected spectra include the K-line of Mg, the L-line of Ag, the L-line of In, and the L-line of Sb. The image pixel density was 512×512 , with a dwell time of 0.01 ms per pixel, repeated 275 times.

Electrical and thermal properties

The electrical conductivity and Seebeck coefficient of the materials were measured using a ZEM-3 commercial setup (Ulvac-Riko, Inc., Japan) in a low-helium atmosphere. The temperature dependence of thermal conductivity was determined according to the relationship $\kappa = D \rho C_p$, where D , ρ , and C_p are thermal diffusivity, density, and specific heat capacity, respectively. A disk-shaped sample with a diameter of -12.7 mm and a thickness of 1–2 mm was polished to measure density using Archimedes' method at room temperature. Subsequently, D was measured by a laser flash method with a commercial system (LFA 457, Netzsch), and C_p was measured using differential scanning calorimetry (DSC-404F3, Netzsch) from room temperature to 553 K. The electrical conductivity and Seebeck coefficient measurements each carry an uncertainty of 5%, resulting in a combined uncertainty of approximately 11% for the power factor. The thermal conductivity has an estimated uncertainty of 7%, accounting for 5% in thermal diffusivity, 5% in specific heat, and 2% in density. Overall, the combined uncertainty in the calculated ZT value is about 13%.

Thermoelectric legs preparation

MgCuSb/MgAgSb/MgCuSb. The MgCuSb/MgAg_{0.97}Sb_{0.99}-0.02InSb/MgCuSb powders were loaded into a graphite die for one-step hot-pressing at 573 K for 30 min under a uniaxial pressure of -80 MPa. The obtained MgCuSb/MgAg_{0.97}Sb_{0.99}-0.02InSb/MgCuSb cylinders with a dimension of -12.7 mm in diameter were cut into squares with an area of $4 \times 4 \text{ mm}^2$.

Fe/Mg_{3.2}Sb₁Bi_{0.995}Te_{0.005}/Fe. The Mg_{3.2}Sb₁Bi_{0.995}Te_{0.005} powder and two Fe foils with a thickness of 300 μm were loaded into a graphite die for one-step hot-pressing at 1073 K for 20 min under a uniaxial pressure of -45 MPa. The obtained Fe/Mg_{3.2}Sb₁Bi_{0.995}Te_{0.005}/Fe cylinders with a dimension of -12.7 mm in diameter were cut into squares with an area of $4 \times 4 \text{ mm}^2$.

Cu/NiCr/Ce_{0.45}Nd_{0.45}Fe_{3.5}Co_{0.5}Sb₁₂. The NiCr powder was synthesized by ball milling Nickel (Ni) powder (99.95%, Aladin) and Chromium (Cr) powder (99.9%, Aladin) at 300 rpm for 4 h using a planetary ball mill. The as-prepared Ni-Cr disk/Ce_{0.45}Nd_{0.45}Fe_{3.5}Co_{0.5}Sb₁₂ powder was loaded into a graphite die for one-step hot-pressing at 903 K for 30 min under a uniaxial pressure of -80 MPa. After that, the obtained Cu/NiCr/Ce_{0.45}Nd_{0.45}Fe_{3.5}Co_{0.5}Sb₁₂ cylinders with a dimension of -12.7 mm in diameter were cut into squares with an area of $4 \times 4 \text{ mm}^2$.

Cu/NiCr/Yb_{0.3}Co₄Sb₁₂-0.05CoSi. Similarly, the Cu powder/as-sintered NiCr disk/ Yb_{0.3}Co₄Sb₁₂-0.05CoSi powder was loaded into a graphite die for one-step hot-pressing at 903 K for 30 min under a uniaxial pressure of -80 MPa. After that, the obtained Cu/NiCr/Yb_{0.3}Co₄Sb₁₂-0.05CoSi cylinders with a dimension of -12.7 mm in diameter were cut into squares with an area of $4 \times 4 \text{ mm}^2$.

Contact resistivity measurement

The interfacial contact resistance (ρ_c) of all junctions was measured using a home-made four-probe measurement system. The as-sintered sandwich-structure bulk, including thermoelectric material and the contact layers, was cut into a regular cuboid shape. Before measurement, the sample surfaces were meticulously polished, and the dimensions were precisely determined. During the measurement, a constant current of 100 mA was applied while the sample was

positioned between two electrodes. The voltage was recorded as the probe scanned along the sample length, traversing both interfaces with a defined step size. The ρ_c was identified by the abrupt increase in voltage at the interface between the thermoelectric material and the contact layer.

Simulation of the theoretical performance of the segmented module

The cross-sectional area (A) of each thermoelectric leg was fixed at $4 \times 4 \text{ mm}^2$ to maximize the fill factor, and the total leg height (L) was maintained at approximately 11.6 mm. This geometry was chosen to collectively minimize parasitic losses arising from thermal radiation and convection between the top and bottom substrates of the device. Temperature-dependent electrical conductivity, Seebeck coefficient, and thermal conductivity of the four materials were employed in the simulation. As the length ratio (R) between the high-temperature and low-temperature legs varied, the segment interface temperature occasionally exceeded the experimentally measured range. To ensure continuity in the simulations, linear interpolation was applied to extend the property data of the low-temperature segment materials up to 773 K. The optimal value of R was subsequently determined based on the resulting temperature distribution across the segment interface.

Thermoelectric module fabrication and characterization

According to simulated optimization results of the dimensions of thermoelectric legs (Fig. 4A), all the pellets were diced into several squares with an area of $4 \times 4 \text{ mm}^2$ using a Wire-Cutting Machine. The joining processes were divided into two steps due to the different service temperatures of the segmented legs. At the first step, the consolidated skutterudite sandwiches with a size of $4 \times 4 \times 8.6 \text{ mm}^3$ were carefully polished to ensure their flatness and parallelism and to obtain similar heights of the legs. A Mo₅₀Cu₅₀ electrode was used to bridge the skutterudite legs using Ag-Cu-Sn-Zn solder. At the second step, the joined high-temperature parts were welded together with Mg-based legs as well as Al₂O₃ ceramic plates using Sn-based solder. The dimension of Al₂O₃ is $10 \times 10 \times 0.65 \text{ mm}^3$. Afterwards, Copper wires are soldered onto the cold-side electrodes for 4-point current and voltage measurements. Then, a full-scale 2-pairs segmented module was prepared (Fig. 1C).

The power generation performance of the MgAgSb/skutterudite segmented module was evaluated using a custom-designed setup under vacuum. A copper block with known thermal conductivity was employed as a heat-flow sensor, with four K-type thermocouples embedded along its length to measure the temperature gradient. The heat flux was determined using the one-dimensional Fourier's law:

$$Q_{out} = \frac{\kappa_{Cu} \times A_{Cu}}{L_{Cu}} \times \Delta T_{Cu} \quad (3)$$

where κ_{Cu} , A_{Cu} , ΔT_{Cu} , and L_{Cu} denote the thermal conductivity, cross-sectional area, length, temperature difference, and vertical distance of the heat-flow meter, respectively. The cold-side temperature was maintained at 293 K using a water-cooling system. To reduce interfacial thermal resistance, graphite paper (0.2 mm) and thermal grease were applied at both the hot-side interface (between heater and module) and the cold-side interface (between module and heat-flow meter). The hot-side and cold-side temperatures (T_H and T_C) were monitored using K-type thermocouples: a 0.5 mm-diameter probe inserted into the heater and a 0.03 mm-diameter wire placed at the interface between the module and Cu block.

Data availability

All data generated or analyzed during this study are included in this published article (and its supplementary information file).

References

1. Yang, J. et al. Next-generation thermoelectric cooling modules based on high-performance $\text{Mg}_3(\text{Bi}, \text{Sb})_2$ material. *Joule* **6**, 193–204 (2022).
2. Xie, L. et al. Lead-free and scalable GeTe-based thermoelectric module with an efficiency of 12%. *Sci. Adv.* **9**, eadg7919 (2023).
3. Ying, P. et al. Performance degradation and protective effects of atomic layer deposition for mg-based thermoelectric modules. *Adv. Funct. Mater.* **34**, 2406473 (2024).
4. Zhang, Q. et al. Micro-thermoelectric devices. *Nat. Electron.* **5**, 333–347 (2022).
5. Qin, Y. X. et al. Grid-plainification enables medium-temperature PbSe thermoelectrics to cool better than Bi_2Te_3 . *Science* **383**, 1204–1209 (2024).
6. Wu, H. J. et al. Broad temperature plateau for thermoelectric figure of merit $ZT > 2$ in phase-separated $\text{PbTe}_{0.7}\text{S}_{0.3}$. *Nat. Commun.* **5**, 4515 (2014).
7. He, W. et al. High thermoelectric performance in low-cost $\text{SnS}_{0.91}\text{Se}_{0.09}$ crystals. *Science* **365**, 1418–1424 (2019).
8. Xiao, Y. & Zhao, L. D. Seeking new, highly effective thermoelectrics. *Science* **367**, 1196–1197 (2020).
9. Beekman, M. et al. Better thermoelectrics through glass-like crystals. *Nat. Mater.* **14**, 1182–1185 (2015).
10. Rowe, D. M. *CRC Handbook of Thermoelectrics*. (CRC Press, 2018).
11. Wu, Y. et al. Lattice strain advances thermoelectrics. *Joule* **3**, 1276–1288 (2019).
12. Poudel, B. et al. High-thermoelectric performance of nanostructured bismuth antimony telluride bulk alloys. *Science* **320**, 634–638 (2008).
13. Dresselhaus, M. S. et al. New directions for low-dimensional thermoelectric materials. *Adv. Mater.* **19**, 1043–1053 (2007).
14. Wang, S. et al. High carrier mobility and promising thermoelectric module performance of N-type PbSe crystals. *Small* **20**, e2400866 (2024).
15. Wang, S. et al. Realizing high-performance thermoelectric modules through enhancing power factor via optimizing carrier mobility in n-type PbSe crystals. *Energ. Environ. Sci.* **17**, 2588–2597 (2024).
16. Ma, X. et al. Single-crystalline $\text{Mg}_3\text{Sb}_{2-x}\text{Bi}_x$ -based thermoelectric materials. *Cell Rep. Phys. Sci.* **5**, 101875 (2024).
17. Ying, P. et al. Hierarchical chemical bonds contributing to the intrinsically low thermal conductivity in α -MgAgSb thermoelectric materials. *Adv. Funct. Mater.* **27**, 1604145 (2017).
18. Li, G. et al. Intrinsic mechanical behavior of MgAgSb thermoelectric material: An ab initio study. *J. Materomics* **6**, 24–32 (2020).
19. Zhang, X. et al. High cooling and power generation performance of α -MgAgSb with intrinsic low lattice thermal conductivity. *Mater. Today Phys.* **44**, 101451 (2024).
20. Bueno Villoro, R. et al. Composite design of half-Heusler thermoelectrics: Selective doping of grain boundary phases in NbFeSb by InSb. *Mater. Today Phys.* **38**, 101240 (2023).
21. Naderloo, R. H. et al. Performance advancements in P-type TaFeSb-based thermoelectric materials through composition and composite optimizations. *Energ. Environ. Sci.* **18**, 738–749 (2025).
22. Tan, G. et al. Toward high thermoelectric performance p-type $\text{FeSb}_{2.2}\text{Te}_{0.8}$ via in situ formation of InSb nanoinclusions. *J. Mater. Chem. C* **3**, 8372–8380 (2015).
23. Yin, Z. et al. Superior carrier mobility enabled by the charge channel leads to enhanced thermoelectric performance in BiCuSeO composites. *Small* **19**, 2304430 (2023).
24. Si, R. et al. Decoupled electron and phonon transport in thermoelectric GeTe compounded with multi-walled carbon nanotubes. *Mater. Today Phys.* **34**, 101081 (2023).
25. Zhao, Y. et al. Decoupling phonon and carrier scattering at carbon nanotube/ Bi_2Te_3 interfaces for improved thermoelectric performance. *Carbon* **170**, 191–198 (2020).
26. Liang, Z. et al. Near-room-temperature thermoelectric performance enhancement via phonon spectra mismatch in $\text{Mg}_3(\text{Sb}, \text{Bi})_2$ -based material by incorporating multi-walled carbon nanotubes. *Adv. Energy Mater.* **13**, 2301107 (2023).
27. Xu, W. et al. Amorphous carbon-modulated $\text{Mg}_3(\text{Bi}, \text{Sb})_2$ and electron-poor CdSb for ultralow-cost Te-free refrigeration modules. *Adv. Funct. Mater.* **35**, 2414194 (2024).
28. Kirkham, M. J. et al. Ab initio determination of crystal structures of the thermoelectric material MgAgSb. *Phys. Rev. B* **85**, 144120 (2012).
29. Huang, Y. et al. Intrinsically high thermoelectric performance in near-room-temperature α -MgAgSb materials. *Acta Mater.* **249**, 118847 (2023).
30. Zhang, X. et al. High-performance MgAgSb/ $\text{Mg}_3(\text{Sb}, \text{Bi})_2$ -based thermoelectrics with $\eta = 12\%$ at $T \leq 583\text{K}$. *Joule* **8**, 3324–3335 (2024).
31. Ying, P. et al. Towards tellurium-free thermoelectric modules for power generation from low-grade heat. *Nat. Commun.* **12**, 1121 (2021).
32. Ying, P. et al. A robust thermoelectric module based on MgAgSb/ $\text{Mg}_3(\text{Sb}, \text{Bi})_2$ with a conversion efficiency of 8.5% and a maximum cooling of 72. *K. Energ. Environ. Sci.* **15**, 2557–2566 (2022).
33. Shuai, J. et al. Study on thermoelectric performance by Na doping in nanostructured $\text{Mg}_{1-x}\text{Na}_x\text{Ag}_{0.97}\text{Sb}_{0.99}$. *Nano Energy* **11**, 640–646 (2015).
34. Ying, P. et al. High performance α -MgAgSb thermoelectric materials for low temperature power generation. *Chem. Mater.* **27**, 909–913 (2015).
35. Sui, J. et al. Effect of Cu concentration on thermoelectric properties of nanostructured p-type $\text{MgAg}_{0.97-x}\text{Cu}_x\text{Sb}_{0.99}$. *Acta Mater.* **87**, 266–272 (2015).
36. Liu, Z. et al. Effects of antimony content in $\text{MgAg}_{0.97}\text{Sb}_x$ on output power and energy conversion efficiency. *Acta Mater.* **102**, 17–23 (2016).
37. Liu, Z. et al. Lithium doping to enhance thermoelectric performance of MgAgSb with weak electron-phonon coupling. *Adv. Energy Mater.* **6**, 1502269 (2016).
38. Liu, Z. et al. The microscopic origin of low thermal conductivity for enhanced thermoelectric performance of Yb doped MgAgSb. *Acta Mater.* **128**, 227–234 (2017).
39. Liu, Z. et al. Mechanical properties of nanostructured thermoelectric materials α -MgAgSb. *Scr. Mater.* **127**, 72–75 (2017).
40. Liu, Z. et al. The influence of doping sites on achieving higher thermoelectric performance for nanostructured α -MgAgSb. *Nano Energy* **31**, 194–200 (2017).
41. Wu, X. et al. Interface engineering boosting high power density and conversion efficiency in $\text{Mg}_2\text{Sn}_{0.75}\text{Ge}_{0.25}$ -based thermoelectric devices. *Adv. Energy Mater.* **13**, 2301350 (2023).
42. Li, H. et al. Ultra-low lattice thermal conductivity realizing ultra-high performance $\text{Bi}_{0.48}\text{Sb}_{1.52}\text{Te}_3$ -based thermoelectric material and module. *Energ. Environ. Sci.* **17**, 6091–6101 (2024).
43. Xie, L. et al. Screening strategy for developing thermoelectric interface materials. *Science* **382**, 921–928 (2023).
44. Wieder, A. et al. High-performance tellurium-free thermoelectric module for moderate temperatures using α -MgAgSb/ $\text{Mg}_2(\text{Si}, \text{Sn})$. *Mater. Today Energy* **38**, 101420 (2023).
45. Wu, X. et al. A high performance eco-friendly MgAgSb-based thermoelectric power generation device near phase transition temperatures. *Energ. Environ. Sci.* **17**, 2879–2887 (2024).
46. Bai, G. et al. Boron strengthened GeTe-based alloys for robust thermoelectric devices with high output power density. *Adv. Energy Mater.* **11**, 2102012 (2021).
47. Fu, Y. et al. $\text{Mg}_3(\text{Bi}, \text{Sb})_2$ -based thermoelectric modules for efficient and reliable waste-heat utilization up to 750 K. *Energ. Environ. Sci.* **15**, 3265–3274 (2022).

48. Shi, W. et al. Batch fabrication and interface stabilization accelerate application of skutterudite thermoelectric module for power generation. *Adv. Energy Mater.* **14**, 2303698 (2024).
49. Zhang, Q. et al. Realizing a thermoelectric conversion efficiency of 12% in bismuth telluride/skutterudite segmented modules through full-parameter optimization and energy-loss minimized integration. *Energ. Environ. Sci.* **10**, 956–963 (2017).
50. Li, W. et al. Bismuth telluride/half-Heusler segmented thermoelectric unicomplex modules provide 12% conversion efficiency. *Adv. Energy Mater.* **10**, 2001924 (2020).
51. Jiang, B. et al. Realizing high-efficiency power generation in low-cost PbS-based thermoelectric materials. *Energ. Environ. Sci.* **13**, 579–591 (2020).
52. Wan, S. et al. High-efficiency segmented thermoelectric power generation modules constructed from all skutterudites. *Cell Rep. Phys. Sci.* **4**, 101651 (2023).
53. Sun, Y. et al. Rational design from materials to devices enables an efficiency of 10.5% based on thermoelectric (Bi, Sb)₂Te₃ and Mg₃(Bi, Sb)₂ for power generation. *En. erg. Environ. Sci.* **17**, 738–747 (2024).
54. Shannon, R. D. Revised effective ionic radii and systematic studies of interatomic distances in halides and chalcogenides. *Acta Cryst.* **32**, 751 (1976).
55. Wang, Q. et al. Multiple effects result in significantly improved thermoelectric figure-of-merit of InSb semiconductors via embedding metastable Ag/Pt nano particles. *Mater. Today Phys.* **27**, 100818 (2022).
56. Li, W. et al. High thermoelectric performance in p-type InSb with all-scale hierarchical architectures. *Mater. Today Energy* **29**, 101091 (2022).
57. Kuo, J. J. et al. Grain boundary dominated charge transport in Mg₃Sb₂-based compounds. *Energ. Environ. Sci.* **11**, 429–434 (2018).
58. Kuo, J. J. et al. Mg deficiency in grain boundaries of n-Type Mg₃Sb₂ identified by atom probe tomography. *Adv. Mater. Interfaces* **6**, 1900429 (2019).
59. Qin, D. et al. Enhanced thermoelectric and mechanical properties in Yb_{0.3}Co₄Sb₁₂ with in situ formed CoSi nanoprecipitates. *Adv. Energy Mater.* **9**, 1902435 (2019).
60. Qu, N. et al. High performance of Mg₃Bi_{1.5}Sb_{0.5} based materials for power generation: revealing the counter-intuitive effect of tuning Bi content on the thermoelectric properties. *J. Magnes. Alloy.* **12**, 4538–4546 (2024).
61. Dong, X. et al. Understanding of isoelectronic alloying induced energy gap variation for a large enhancement of thermoelectric power factor. *Phys. Rev. B* **109**, 155203 (2024).
62. Qu, N. et al. Interfacial design contributing to high conversion efficiency in Mg₃(Sb, Bi)₂/Bi₂Te₃ thermoelectric module with superior stability. *Adv. Energy Mater.* **14**, 2302818 (2023).
63. Ying, P. et al. Geometrical optimization and thermal-stability characterization of te-free thermoelectric modules based on MgAgSb/Mg₃(Bi, Sb)₂. *Small* **18**, e2201183 (2022).
- Foundation of Heilongjiang Province (LH2023E032, awarded to Z.L.) and the State Key Laboratory for Mechanical Behavior of Materials (20232507, awarded to Z.L.).

Author contributions

L.X., Z.L., and J.S. initiated the concept and designed this project. L.X., H.T., W.S., K.Y., J.H., L.J., and X.D. prepared the samples, performed the thermoelectric property measurements, and fabricated the TE module. L.X. and Hao Wu established the model for the transport properties of the module. G.P., Y.Z., and Haijun Wu performed the STEM study. Hao Wu measured the power generation performance of modules. L.X., Z.L., F.G., W.C., and J.S. analyzed the results. All authors edited the manuscript. All the authors reviewed, discussed, and approved the results and conclusions.

Competing interests

The authors declare no competing interests.

Additional information

Supplementary information The online version contains supplementary material available at <https://doi.org/10.1038/s41467-025-62902-8>.

Correspondence and requests for materials should be addressed to Haijun Wu, Zihang Liu or Jiehe Sui.

Peer review information *Nature Communications* thanks the anonymous, reviewer(s) for their contribution to the peer review of this work. A peer review file is available.

Reprints and permissions information is available at <http://www.nature.com/reprints>

Publisher's note Springer Nature remains neutral with regard to jurisdictional claims in published maps and institutional affiliations.

Open Access This article is licensed under a Creative Commons Attribution-NonCommercial-NoDerivatives 4.0 International License, which permits any non-commercial use, sharing, distribution and reproduction in any medium or format, as long as you give appropriate credit to the original author(s) and the source, provide a link to the Creative Commons licence, and indicate if you modified the licensed material. You do not have permission under this licence to share adapted material derived from this article or parts of it. The images or other third party material in this article are included in the article's Creative Commons licence, unless indicated otherwise in a credit line to the material. If material is not included in the article's Creative Commons licence and your intended use is not permitted by statutory regulation or exceeds the permitted use, you will need to obtain permission directly from the copyright holder. To view a copy of this licence, visit <http://creativecommons.org/licenses/by-nc-nd/4.0/>.

© The Author(s) 2025

Acknowledgements

This work was funded by the National Natural Science Foundation of China (Nos. U23A20556 awarded to J.S., 52472250 and 52172128 awarded to H.W.). Thanks to the support from the Natural Science